ELSEVIER

Polymer 44 (2003) 1871–1879

polymer

www.elsevier.com/locate/polymer

Geometric phase analysis of lattice images from algal cellulose microfibrils

Tomoya Imai[a], Jean-Luc Putaux[b,*], Junji Sugiyama[a]

[a]*Wood Research Institute, Kyoto University, Uji, Kyoto 611-0011, Japan*
[b]*Centre de Recherches sur les Macromolécules Végétales, CNRS, BP 53, 38041 Grenoble Cedex 9, France*

Received 15 May 2002; received in revised form 7 November 2002; accepted 13 November 2002

Abstract

A geometric phase analysis has been applied to high-resolution transmission electron microscopy images from algal cellulose microcrystals. The pictures were decomposed into images containing selectively the amplitude or phase information associated to selected Bragg reflections. Compared with I_β (monoclinic)-rich cellulose microfibrils, I_α(triclinic)-rich microfibrils were found to be more heterogeneous when viewed along the H-bonding sheets. As a microfibril twist and radiation damage could not be totally ruled out as having an effect on the lattice image, this result has to be considered with care when used in order to survey the distribution of different allomorphs in a cellulose microfibril. However, the geometric phase analysis of noisy low dose high-resolution images appears as a promising new method to investigate polymer crystals and the distribution of domains having different structures or containing lattice distortions.

Keywords: Cellulose I; Lattice imaging; Geometric phase

1. Introduction

High-resolution transmission electron microscopy (HRTEM) is a very powerful tool to study the structure of crystalline materials at the nanometric scale. With this technique, images directly showing projections of the crystal lattice have proven invaluable to describe the atomic or molecular organization of a number of specimens. The recording of these images relies on the use of high magnifications and therefore requires substantial electron doses. While the technique is well adapted to study beam-resistant inorganic materials (metals, ceramics, semiconductors, etc.), for beam-sensitive specimens such as crystalline polymers or biological objects, the recording of lattice images can only be achieved at low or medium magnification—typically below 50,000 ×—using very low electron doses.

Applying HRTEM imaging to beam-sensitive specimens is still a substantial challenge. Given the nature of beam-sensitive samples and the conditions that are required to obtain meaningful HRTEM images, a number of procedures and tools have been developed to optimize the recording of such images. The 'low dose' procedure, which is implemented in all recent transmission electron microscopes, is one of them. It allows setting the focus at an area nearby the region of interest to prevent any unnecessary irradiation prior to actual image recording. However, at magnifications below 50,000 ×, it is quite difficult to control and therefore insure optimal high-resolution imaging (e.g. set the defocus at the Scherzer value). The use of cryo-specimen holders operated either at liquid nitrogen or liquid helium temperature is another way to reduce the detrimental effect of beam damage. Despite these advances, most lattice images produced so far from beam-sensitive specimens have been highly underexposed and therefore exhibit a very low signal-to-noise ratio (S/N). A consequence is that it is often difficult to measure their defocus precisely.

Considerable effort has been made to interpret low S/N lattice images from fragile specimens such as protein 2D crystals [1,2] and synthetic polymers [3,4]. Crystalline polysaccharides are among the most-sensitive polymers when irradiated by highly accelerated electrons. Nevertheless, lattice images have been obtained by several authors to visualize the molecular structure of a number of

* Corresponding author. Tel.: +33-476037604; fax: +33-476547203.
E-mail address: putaux@cermav.cnrs.fr (J.L. Putaux).

0032-3861/03/$ - see front matter © 2002 Elsevier Science Ltd. All rights reserved.
PII: S0032-3861(02)00861-3

polysaccharide crystals [5]: cellulose [6–11] or chitin microfibrils [12–15], chitin [16] and amylose [17] single crystals. In these images, lattice information up to 0.35–0.39 nm have been recorded, both at low and room temperature.

The extraction of meaningful information from HRTEM images with low S/N requires extensive image processing. Bragg filtering is one of the methods that are commonly used to enhance the periodic signal that is present in the image, while ignoring the statistical background noise. This procedure requires particular care if one wants to avoid—or at least monitor—the artefacts that might be introduced during the calculations [18,19]. A new computing technique has been recently introduced by Hÿtch and co-workers [20,21]. This method is based on the analysis of the geometric phase information in lattice images and is particularly adapted to detect and measure the size of crystalline domains in complex materials. It has been successfully applied to HRTEM images of a number of beam-resistant specimens: cadmium sulfide nanocrystals embedded in an amorphous matrix [20], carbon nanotubes [21], antiphase domains in Cu_3Au [22] and domains in ferroelectric materials [23]. The method has also proven quite powerful to quantitatively measure atomic displacement fields from HRTEM images [24,25]. However, to our knowledge, it has never been applied to low S/N lattice images of beam-sensitive specimens.

In this work, we have used the geometric phase analysis to study the distribution of crystalline domains in native cellulose microfibrils from *Cladophora*. This algal cellulose, which is highly beam sensitive, is known to be a composite of two allomorphs, namely triclinic I_α and monoclinic I_β (Fig. 1) [26,27]. Their distribution pattern in a microfibril is complex and depends on the sample origin. Both allomorphs alternate longitudinally in *Microdictyon* [27] while the alternation is both longitudinal and lateral in *Cladophora* and other green marine algae [28]. Electron diffraction experiments have provided some hints on the distribution of I_α and I_β phases in these specimens [27,28]. The processing of HRTEM images using the geometric phase analysis is expected to corroborate the electron diffraction results and provide additional information at the lattice resolution.

2. Experimental details

2.1. Sample preparation

Cladophora, a green marine alga, was harvested at sea bed in Chikura, Chiba, Japan. It is known to contain highly crystalline I_α-rich cellulose. After ethanol extraction, the cell wall was purified by boiling in 0.1 N aq. NaOH for 5 h and immersed in 0.05 N HCl at room temperature for 12 h. Some samples of the purified cell wall were annealed to I_β-rich cellulose by a hydrothermal treatment [29]. Our previous survey by infrared spectroscopy provided I_α fractions of 0.76 and 0.24 for initial and annealed *Cladophora*, respectively [28]. Specimens for dark field (DF) imaging were prepared as follows: under a stereomicroscope, the cell wall was delaminated using a pair of tweezers. A uniaxially oriented lamella was thus obtained and deposited on a carbon-coated copper grid. For HRTEM, these specimens were disintegrated into microcrystals by acid hydrolysis in 40% H_2SO_4 at 70 °C for 12 h with stirring. The cellulose microfibrils obtained by centrifugal washing and dialysis with distilled water had a length of several micrometers and a thickness of 20–30 nm [28]. A drop of the suspension was allowed to dry on a gold-coated holey carbon microgrid [30] supporting a ultra-thin continuous carbon film.

2.2. Electron microscopy

DF micrographs were obtained using a JEOL JEM 2000EX II microscope operated at an accelerating voltage of 100 kV and a magnification of 5000×. A 100 μm objective aperture was inserted in the back focal plane to select any of the following reflections: 110_t, $010_t/100_t$, and $\bar{1}\bar{1}4_t$.[1] In particular, in order to record the $(110)_t$ DF image, the specimen was tilted by 40° around the fiber axis to bring the corresponding lattice planes into Bragg condition. No tilting was used for the other reflections.

For HRTEM, the samples were observed using a Philips CM200 'Cryo' microscope operated at 200 kV. As the stability of the cold specimen holder available was not good enough to ensure a correct imaging of the cellulose lattice planes at liquid nitrogen temperature, we worked at room temperature using a single-tilt side-entry specimen holder. Lattice images were recorded using the Philips 'Low Dose System' which allows to set up the imaging conditions near the area of interest in order to protect it from any damaging irradiation prior to photographic exposure. Areas with microfibrils were first selected at low magnification (1000×) and focus was set at a magnification of 27,500×, at a distance of 3 μm from the region of interest. The beam was then blanked until the image was actually recorded at magnifications of 27,500× and 38,000×, on Agfa Scientia films.

2.3. Image processing

The original negatives were first sorted out using laser diffractometry on an optical bench in order to rapidly select the pictures exhibiting diffracting areas. Special care was taken to calibrate the optical diffraction spots and sort the regions of interest depending on the type of reflection that

[1] Throughout this paper, the indexation of the crystallographic planes refers to the model of Sugiyama et al. [27] where the three major equatorial planes are indexed in the triclinic (t) or monoclinic (m) unit cell as: $(100)_t/(1\bar{1}0)_m$, $(010)_t/(110)_m$ and $(110)_t/(200)_m$ with corresponding d-spacings of 0.62/0.60, 0.53/0.54 and 0.39/0.40 nm, respectively (Fig. 1).

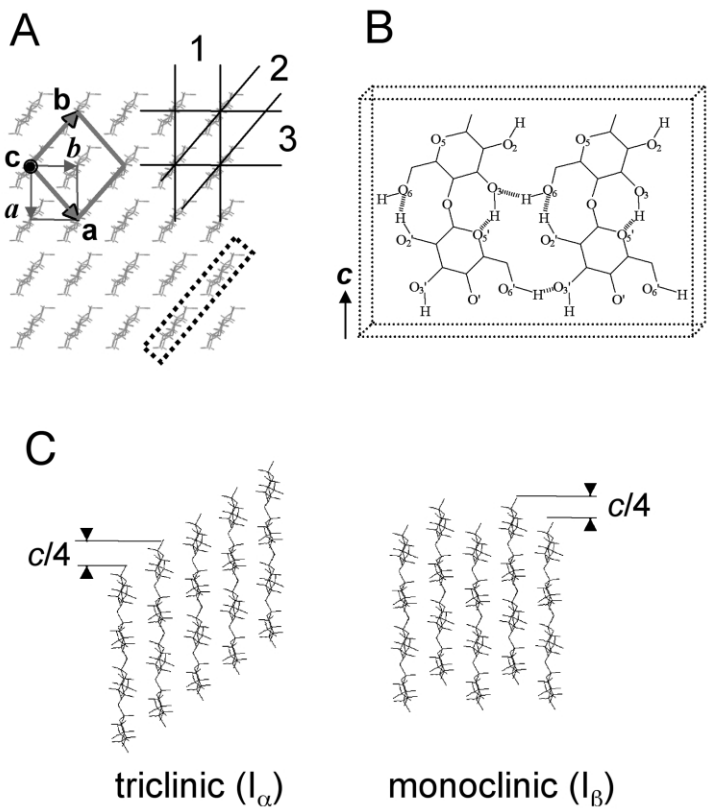

Fig. 1. Current structural model of crystalline native cellulose. (A) Cross-sectional view of a cellulose I crystal. The unit cells of I_α and I_β crystals are shown by thin and bold lines, respectively. Viewed along this direction, both share a nearly identical molecular arrangement: three major families of lattice planes, numbered 1, 2 and 3, are seen in both structures, with d-spacings of 0.61, 0.53 and 0.39 nm, respectively. As outlined in the dotted box, sheets are formed by molecular chains stabilized by the network of H-bondings described in (B) [36,37]. There are two intramolecular and one intermolecular H-bondings. (C) Cellulose I crystals viewed along $[1\bar{1}0]_t/[010]_m$ axes. The translation vector of the H-bonding sheets is $c/4$ along the chain axis for I_α, while it is alternatively $c/4$ and $-c/4$ for I_β.

was observed. The selected areas were then enlarged and digitized using an 8 bits black and white Kodak Megaplus digital CCD camera. Samplings of 0.14 and 0.19 nm/pixel were achieved for corresponding magnifications in the original negatives of 38,000 × and 27,500 ×, respectively. The numerical images were transferred either in a desktop computer equipped with a Pentium processor or a Silicon Graphics workstation and processed using the Semper 6.4 program [31] (Synoptics, UK).

3. Image decomposition and geometric phase image analysis

A digital image is a network of pixels which can be defined by their position **r** and intensity **I**(**r**), also called gray level. In the Fourier transform of the image, pixels have the position **f** (spatial frequency) and intensity $\tilde{I}(\mathbf{f})$. If an image contains periodical signals, its Fourier transform reveals a symmetrical pattern of strong frequency components **g**, the Bragg reflections [32]. Practically, these components are more easily detected in the power spectrum (PS) of the image, i.e. the real function $|I(\mathbf{r}) \times \tilde{I}(\mathbf{f})|$, but the calculations are performed on the Fourier transform $\tilde{I}(\mathbf{f})$. By masking the frequencies around a Friedel pair of symmetrical reflections $\pm\mathbf{g}$ and performing an inverse Fourier transform, a Bragg filtered image is obtained in which the lattice lines associated to $\pm\mathbf{g}$ are enhanced:

$$B_{\mathbf{g}}(\mathbf{r}) = 2A_{\mathbf{g}}(\mathbf{r})\cos[2\pi\mathbf{g}\cdot\mathbf{r} + P_{\mathbf{g}}(\mathbf{r})] \quad (1)$$

where $A_{\mathbf{g}}$ is the amplitude of the signal and $P_{\mathbf{g}}$ its phase, i.e. the positional information with respect to an origin.

Although Bragg filtering is easy to carry out, it may, in the case of low S/N images, induce artifacts which mostly depend on the diameter of the filtering mask that is applied. Let us consider the specific case of a crystalline fiber deposited on an amorphous supporting film. In lattice images, the corresponding periodical signal is finite, extending only over the fiber width. In the Fourier transform of the image, the information about the position of the fiber borders is distributed in the vicinity of the reflections corresponding to the lattice planes [33]. If the mask used for the filtering is too small, this information may be lost in the Bragg image and the signal may extend out of the geometrical limits of the fiber, thus increasing its apparent width. This effect has been described in detail by Pradère and Thomas [19] who called the artefact 'ghost lattice'.

Another important artifact arises due to the very high

noise level in polymer HRTEM images. In the case of polysaccharides, S/N is less than 5% in most cases, as estimated using the method by Stewart [34]. Using the previous example, we can assume, at first approximation, that the lattice image of the fiber is the sum of periodic signals and random noise. In the Fourier space, the information about noise is scattered everywhere. The mask used to select the strong reflection also includes a certain amount of information related to noise. If S/N is very low, the influence of this noise component is not negligible, and the lattice fringes in the Bragg image fluctuate in intensity and spacing. As shown by Pradère et al. [18] and Pradère and Thomas [19], lattice 'dislocations' may sometimes be observed, their position depending on the diameter of the filtering mask or the proportion of noise included. These dislocations are artefactual and do not correspond to actual structural defects.

Consequently, the choice of the diameter of the mask is critical for the Bragg filtering of low S/N lattice images, as preserving relevant structural information (here the width of the fiber) may at the same time emphasize the contribution of the noise. Considering the limitation of Bragg filtering specifically applied to low S/N images, it was interesting to use another approach that did not depend so strongly on the filtering conditions. In the method described by Hÿtch and Gandais [20], the function $P_{\mathbf{g}}(\mathbf{r})$ in expression (1) is analyzed in detail. It has to be emphasized that this phase is not that of the electron wave function emerging from the crystal but the information related to the position of the lattice fringes contained in an HRTEM image with respect to a fixed origin. For this reason, Hÿtch and Gandais preferred using the term 'geometric phase' [20].

The specifics and formalism of the phase image analysis method have been extensively described by Hÿtch and Gandais [20], Hÿtch [21], Hÿtch and Potez [22], and Hÿtch et al. [23]. Only a summary is presented in the following. As opposed to the Bragg filtering procedure where a Friedel pair of reflections $\pm\mathbf{g}$ is selected, here a circular mask is applied around a single reflection $\mathbf{g}$ in the complex full-plane Fourier transform of the original lattice image. Then, the term $2\pi\mathbf{g}\cdot\mathbf{r}$ is subtracted, a procedure equivalent to recentering the Fourier image around $\mathbf{g}$. The result is back Fourier transformed. A new image, which is a complex function, is obtained from which the corresponding amplitude $A_{\mathbf{g}}(\mathbf{r})$ and phase $P_{\mathbf{g}}(\mathbf{r})$ are then calculated. As Semper can handle complete images in its calculations, using the proper set of commands allows visualizing the amplitude and phase information and their variation throughout the whole image. The phase image that is finally analyzed is obtained after rescaling the intensities between $-\pi$ (black) and π (white).

The advantage of this method is that the phase information is rather insensitive to noise, as explained by Hÿtch and Gandais [20]. Moreover, while retrieving $A_{\mathbf{g}}(\mathbf{r})$ provides an information similar to that brought by DF imaging, the analysis of the local phase variations $P_{\mathbf{g}}(\mathbf{r})$ reveals interesting additional structural results. For instance, let us consider a small variation of the lattice spacing that corresponds to a variation $\Delta\mathbf{g}$ in the reciprocal space. A Bragg image obtained using a mask with a radius larger than $\Delta\mathbf{g}$ will be described by expression (1) re-written for $\mathbf{g}+\Delta\mathbf{g}$:

$$B_{\mathbf{g}}(\mathbf{r}) = 2A_{\mathbf{g}}(\mathbf{r})\cos[2\pi\mathbf{g}\cdot\mathbf{r} + 2\pi\Delta\mathbf{g}\cdot\mathbf{r} + P_{\mathbf{g}}(\mathbf{r})] \quad (2)$$

A uniform ramp $2\pi\Delta\mathbf{g}\cdot\mathbf{r}$ is thus added to the phase term. If the filtering mask has been centered on $\mathbf{g}$, the contribution of this additional term can be detected in the phase image as a gradient of gray levels. This means that a gradient of phase can be related to a variation in the reciprocal lattice vector $\mathbf{g}$, hence a local change in the spacing of the corresponding lattice planes.

In HRTEM images of radiation-sensitive specimens, the lattice spacing does not remain constant across the whole field of view, mostly due to crystal imperfections, misorientations and radiation damage. Thus, the choice of the position of reflection $\mathbf{g}$ is just arbitrary and corresponds to an average over domains. Practically, the position of the filtering mask is chosen in the PS of the image by calculating the center of mass around the Bragg reflection whose intensity is generally distributed over a group of neighboring pixels.

Micrographs of cellulose microfibrils are presented in Figs. 3–5. The aspect of amplitude and phase images is quite typical of what is obtained with very noisy lattice images. In the amplitude images (Figs. 3(C), 4(C) and 5(C)), the brighter the intensity, the higher the amplitude of the lattice fringes. Two domains with different but close lattice spacings or shifted with respect to one another would both appear as bright areas. In that respect, the information that is retrieved in amplitude images is very similar to that visualized on DF micrographs such as those presented in Fig. 2. DF or amplitude images alone cannot be used to

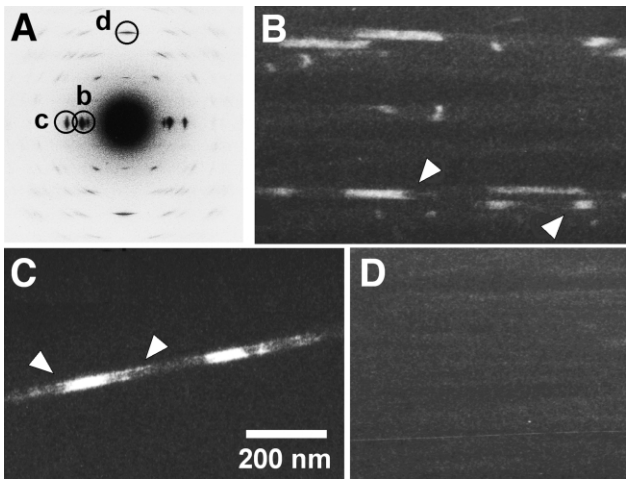

Fig. 2. Typical dark-field images of cellulose microfibrils, formed by selecting equatorial $100_t + 010_t$ (B), 110_t (C), and meridional $\bar{1}\bar{1}4_t$ (D) reflections in the cellulose I diffraction diagram (A). The bright regions in each DF image correspond to the reflections circled in (A) (b–d).

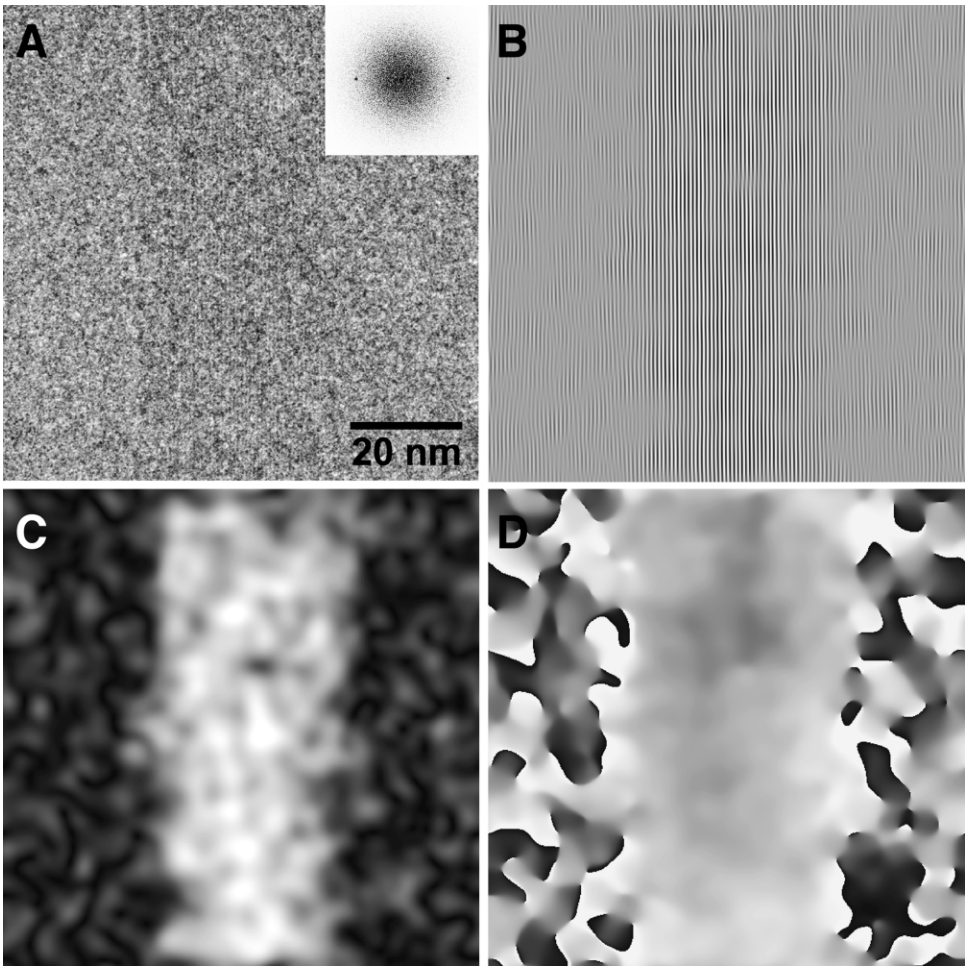

Fig. 3. (A) Longitudinal lattice image of $(010)_t$ planes from a I_α-rich *Cladophora* cellulose microfibril. Inset is the corresponding power spectrum. (B)–(D) Corresponding Bragg-filtered, amplitude and geometric phase images, respectively.

differentiate domains with different but close lattice spacings.

In phase images, domains with lattice fringes are identified by a more or less constant gray level whereas amorphous regions are recognized by a randomly fluctuating intensity with sharp transitions from white to black (Figs. 3(D), 4(D) and 5(D)). These transitions are a consequence of the renormalization of the phase between $-\pi$ and π. A phase of $\pi + \epsilon$ (ϵ small) will be renormalized to $-\pi + \epsilon$. If two domains have identical lattice spacings $1/|\mathbf{g}|$ but are translated with respect to one another, the PS will exhibit one strong reflection $\mathbf{g}$. However, the average phases of each domain will be different and phase image will show the two domains with different gray levels. The phase shift equals π when the translation is half the lattice spacing (or an odd multiple). If two domains have different lattice spacings or if they are rotated with respect to one another, two reflections are observed in the PS. If one of two very close spots is chosen as a reference to center the filtering mask, the formalism of expression (2) can be applied: in the phase image, the domain corresponding to the reference reflection exhibits a constant gray level and the other domain appears as a ramp of grays. In addition, the direction of the ramp in the image and that of $\Delta\mathbf{g}$ in the diffractogram will match. If an average position in-between both reflections are chosen, then both domains will exhibit gradients of grays.

The lateral resolution of the analysis is directly related to the size of the filtering mask which, ideally, should be chosen in order to filter the image at a scale of one unit cell [20]. However, for low S/N images, the size of such an ideal mask would imply incorporating a high proportion of noise which would certainly induce several filtering artefacts [18]. Moreover, the use of a smaller mask corresponds to an averaging over a larger surface in the image. This improves the readability of the phase images by leveling to some extent the sharp transitions of the local phase. In our calculations, we set the mask radius to $|\mathbf{g}|/16$, the priority being given to the readability of the phase image at the expense of resolution. This corresponds to an averaging over 16 lattice fringes in the real image.

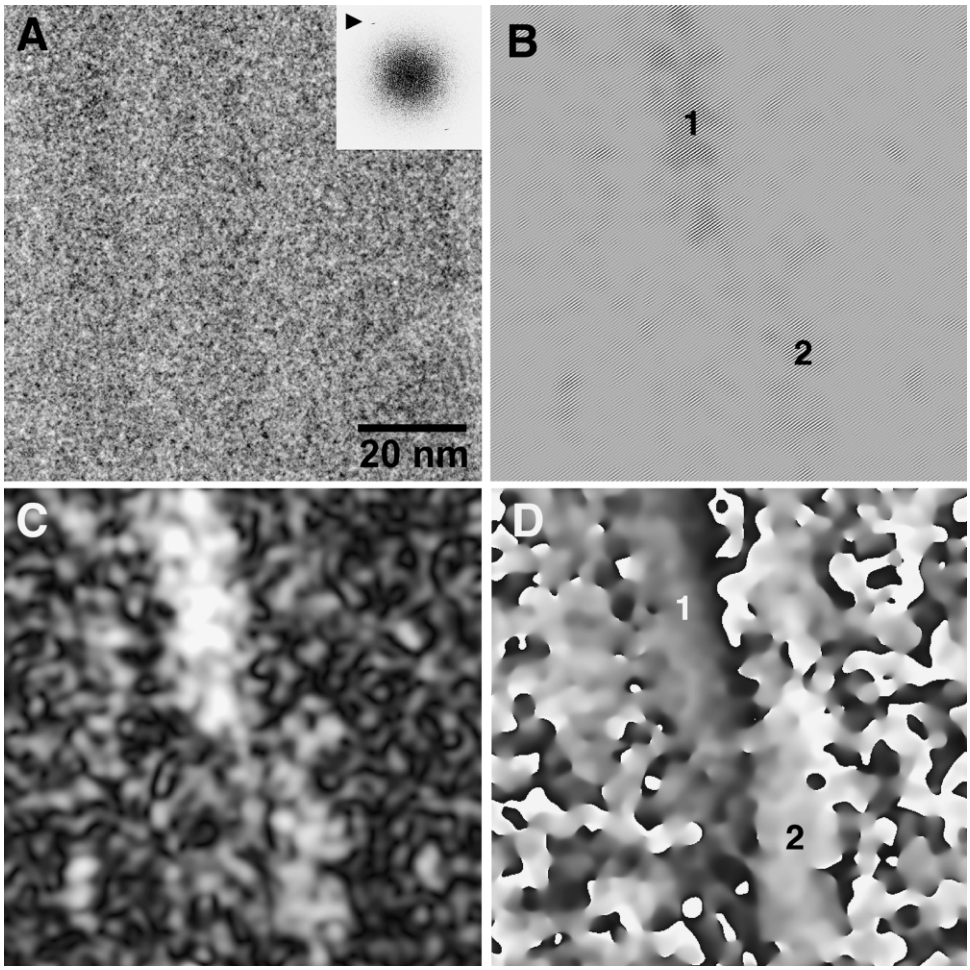

Fig. 4. (A) Longitudinal lattice image of $(110)_t$ and $(\bar{1}\bar{1}2)_t$ planes from a I_α-rich *Cladophora* cellulose microfibril. Inset is the corresponding power spectrum with arrowhead indicating the $\bar{1}\bar{1}2_t$ reflection. (B)–(D) Bragg-filtered, amplitude and geometric phase images of $(\bar{1}\bar{1}2)_t$ planes, respectively. In (B) and (D), 1 and 2 refer to different crystal domains.

4. Results

Bourret et al. [35] used DF imaging to investigate *Valonia* cellulose microcrystals. To form DF images, they selected all three equatorial reflections in the objective aperture. In our experiments, we have used the following reflections: 110_t as well as 100_t and 010_t. The latter two could not be separated because no small enough objective aperture was available (Fig. 2(A)). As the microfibrils have a preferential orientation on the supporting carbon film, 010_t is generally the most intense reflection. The corresponding DF images can thus be regarded as primarily due to the diffraction of the $(010)_t$ lattice planes.

Fig. 2 shows typical DF images (B–D) together with selected-area electron diffraction diagrams (A) recorded from the same sample preparation. The crystalline areas satisfying the Bragg condition are bright. In the image corresponding to the meridional $\bar{1}\bar{1}4_t$ reflection (Fig. 2(D)), the contrast is uniform along the microfibrils, although the signal is very weak. This means that the fibers lie rather flat on the supporting carbon film so that the meridional planes remain in Bragg condition along a large length. Conversely, in Fig. 2(B) and (C), the diffracting areas are of limited lengths. A slight rotation about the microfibril axis would deviate equatorial planes off Bragg condition (a 3° deviation is enough to observe a complete loss of diffraction intensity [9]) but meridional planes would remain in Bragg orientation. Consequently, as the reflections selected in the objective lens aperture correspond to equatorial planes, the variation in contrast is likely due to some local twist of the specimen rather than to any discontinuity in the crystal lattice.

While DF images are useful to get an overview of the diffracting areas, the direct visualization of the lattice planes by HRTEM is expected to provide additional local information. The procedure described in Section 3 was carried out to retrieve the amplitude and phase images from our experimental HRTEM micrographs of cellulose microfibrils.

Fig. 3 shows the $(010)_t$ lattice image of *Cladophora* cellulose (A) and the corresponding image decomposition (B–D). High amplitude and a rather stable phase were retrieved along a long region of the microcrystal (Fig. 3(C)

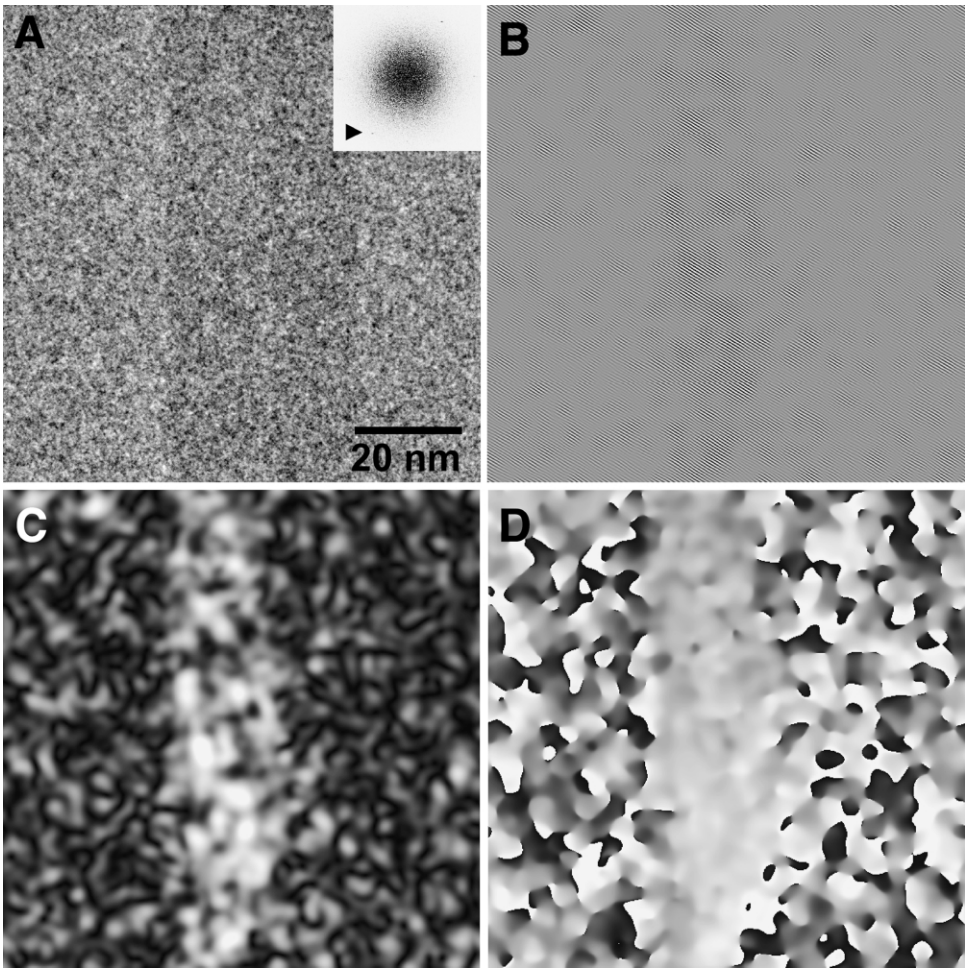

Fig. 5. (A) Longitudinal lattice image of $(102)_m$ planes from a I_β-rich annealed *Cladophora* cellulose microfibril. The projection is equivalent to that in Fig. 4. Inset is the corresponding power spectrum. (B)–(D) Corresponding Bragg-filtered, amplitude and geometric phase images, respectively.

and (D)). Such a homogeneous region sometimes extended over a length of 500 nm or more. This indicates that the signal is uniform, as also shown in the Bragg filtered image of Fig. 3(B). This means that the $(010)_t$ lattice planes, which correspond to the molecular sheets formed by van der Waals bonding [27,36,37] (Fig. 1), are well ordered. We drew a similar conclusion from I_β-dominant hydrothermally treated specimens which provided well-ordered $(110)_m$ fringes (not shown).

Fig. 4(A) shows an HRTEM image of *Cladophora* along the $[1\bar{1}0]_t$ axis. The lattice fringes in the initial image are hardly visible, as confirmed by the low amplitude in Fig. 4(B). The PS contains both 110_t and $\bar{1}\bar{1}2_t$ reflections. We focused our study on the lattice fringes corresponding to the latter reflection which had a higher amplitude. Moreover, a careful examination of PSs from different lattice images showed that the $\bar{1}\bar{1}2_t$ spot was generally splitted (Fig. 6(B)). Such an effect was only detected in HRTEM images of native *Cladophora* cellulose. The Bragg filtered image in Fig. 4(B) as well as the amplitude image in Fig. 4(C) show that the $(\bar{1}\bar{1}2)_t$ lattice fringes are not visible over the whole microcrystal but are distributed in separate regions. Two domains with different average phase values can be seen in Fig. 4(D).

We compared the images in Fig. 4 with those recorded from I_β-rich annealed *Cladophora* cellulose (Fig. 5). Both

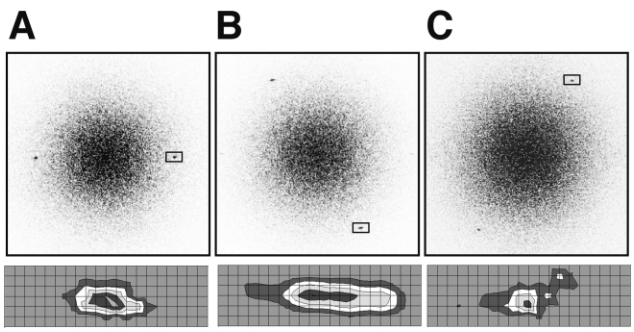

Fig. 6. Typical power spectra from lattice images recorded along different directions. (A) 010_t spots from I_α-rich *Cladophora* cellulose. (B) $\bar{1}\bar{1}2_t$ spots from I_α-rich *Cladophora* cellulose. (C) 102_m spots from I_β-rich annealed *Cladophora* cellulose. The rectangles below contain enlargements of selected reflections drawn in intensity contours.

the amplitude and geometric phase images of $(102)_m$ lattice planes, which correspond to the $(\bar{1}\bar{1}2)_t$ planes in initial I_α-rich *Cladophora* cellulose, show intensities that are more continuous along the microfibril. In addition, the 102_m reflection in the PS is spot-like (Fig. 6(C)).

5. Discussion

In a previous work [28], Imai and Sugiyama analyzed electron microdiffraction diagrams recorded on I_α-rich and I_β-rich algal cellulose microfibrils. A split of some reflections was observed in the diagrams of I_α-rich cellulose recorded along $[1\bar{1}0]_t$ exclusively. The splitting effect was interpreted as due to the superimposition of diffraction patterns of the I_α and I_β allomorphs. A structural model for cellulose I based on the coexistence of I_α and I_β nanodomains across a single cellulose microfibril was proposed. The length of the microfibrils that was probed by microdiffraction was directly defined by the size of the electron probe that was used in this work, namely 100 nm. HRTEM imaging is expected to provide local information on the distribution of domains with a resolution of the order of a unit cell.

The geometric phase analysis of our HRTEM images brought several results: (i) the $(010)_t$ and $(110)_m$ lattice images of I_α-rich and I_β-rich *Cladophora* cellulose exhibited homogeneous phases along the microcrystals; (ii) separate domains were observed in $(\bar{1}\bar{1}2)_t$ lattice images of I_α-rich *Cladophora* cellulose; (iii) the geometric phase of the corresponding $(102)_m$ lattice images of I_β-rich annealed *Cladophora* cellulose were homogeneous along the microfibrils. These results are consistent with those obtained from electron microdiffraction [28] as separate domains were only detected in images of I_α-rich *Cladophora* cellulose recorded along $[1\bar{1}0]_t$. Domains 1 and 2 shown in Fig. 4(D) have different average phases which means that one is shifted with respect to the other by a distance which is not an exact multiple of one lattice spacing. According to the formalism of Section 3, if one domain is chosen as a reference (by centering the filtering mask on the corresponding reflection), a phase gradient should appear in the second domain. As a matter of fact, it is difficult to decide if such a gradient can be unambiguously seen in our image. The radius of the averaging mask was chosen to be $|\mathbf{g}|/16$. Consequently, the corresponding 'averaging unit' in the real space extends over 16 lattice fringes. As the detected domains had a small lateral size, we considered that the calculation of the phase gradient could not be performed over a sufficient number of 'averaging units' and therefore could not be reliable. Improving resolution would require increasing the diameter of the mask and thus including more noise in the averaging process, resulting in more distorted phase information. One may see here the limit of our geometric phase analysis. Nevertheless, the resolution of this method is still better than that of the microdiffraction technique.

Using molecular dynamics simulations, Cousins and Brown [38] proposed a two-step model describing the biosynthesis and crystallization of cellulose microfibrils. First, molecular chains of cellulose are assembled by van der Waals forces to form 'mini-sheets' which are subsequently packed by both van der Waals interaction and H-bonding into a crystal with a rectangular section. Fig. 3 is a projection of the $(010)_t$ lattice planes. Consequently, it directly shows the packing of the mini-sheets. As the geometric phase of the 010_t reflection appears to be homogeneous along a large portion of the microfibril, we would conclude that the conjunction of van der Waals force and H-bonding yields a regular packing of the mini-sheets. However, as shown on the structural models in Fig. 1, both I_α and I_β crystals can also be described by specific packings of molecular sheets stabilized by H-bonding [27]. Fig. 1(C) shows how the sheets are translated with respect to one another by $c/4$ along the chain axis for the triclinic model while the translation alternates ($+c/4$ and $-c/4$) for the monoclinic crystal. The speculative model proposed by Imai and Sugiyama to describe the structure of native cellulose suggests that I_α and I_β domains alternate longitudinally and laterally along one microfibril [28]. The interface separating domains that coexist laterally is controlled by the $\pm c/4$ translations between the H-bonding sheets along the chain axis. As the H-bonding sheets are packed by weaker van der Waals interactions, one can expect imperfections in the packing resulting in 'defects' that would be visible in HRTEM images recorded along $[1\bar{1}0]_t$. The domain structure revealed by the geometric phase image of the $(\bar{1}\bar{1}2)_t$ lattice planes (Fig. 4(D)) is consistent with such a model.

The comparison of the geometric phase images of native I_α-rich and annealed I_β-rich cellulose microfibrils (Fig. 4(D) and 5(D), respectively) recorded along $[1\bar{1}0]_t/[010]_m$ indicates that the imperfect stacking of the H-bonding sheets in I_α-rich cellulose disappears after a hydrothermal treatment. Annealing improves the homogeneity of the molecular packing by allowing the H-bonding sheets to translate along the chain axis: I_α cellulose transforms into the thermodynamically more stable I_β allomorph [29].

Our results are consistent with the working model of Imai and Sugiyama [28] that suggests that the crystal structure is controlled by the translations of H-bonding sheets along the chain axis rather than the packing of mini-sheets [38]. However, additional experiments are necessary to record several more micrographs and improve the statistics of our study. To minimize radiation damage and its distorting effect on the crystal lattice, the use of liquid helium temperature in conjunction with a higher acceleration voltage has to be considered [39]. The mechanical stability and electrical conductivity at very low temperature may also be improved by 'sandwiching' the sample between two ultra-thin carbon films [40,41].

6. Conclusion

The geometric phase image analysis is a promising method to retrieve local structural information from highly noisy HRTEM micrographs of radiation-sensitive specimens, such as polymers that are polyphasic—or simply polycrystalline—at the nanometric scale. Although our results obtained from lattice images of cellulose I microfibrils seem to corroborate those from electron microdiffraction experiments, they have to be considered as preliminary, as they certainly need to be supported by many additional observations along different projections of the crystals. Moreover, in this work, the influence of imaging conditions, specimen tilt or radiation damage has not been taken into account. Such effects, which can induce distortions in the lattice images, should be considered with care in a future study.

Acknowledgements

This study was supported by a Joint Research Program between the Japanese Society for the Promotion of Science (JSPS) and the Centre National de la Recherche Scientifique (CNRS). One author (T.I.) was a recipient of a JSPS fellowship. We are also indebted to Dr Hÿtch (Centre d'Etude de Chimie Métallurgique—CNRS, Vitry, France) for introducing us to the geometric phase image analysis method, for his help in the use of Semper and for his critical reading of the manuscript.

References

[1] Henderson R, Gleaser RM. Ultramicroscopy 1985;16:139–50.
[2] Henderson R, Baldwin JM, Downing KH, Lepault J, Zemlin F. Ultramicroscopy 1986;19:147–78.
[3] Martin DC, Thomas EL. Polymer 1995;36:1743–59.
[4] Tsuji M, Kohjiya S. Prog Polym Sci 1995;20:259–308.
[5] Perez S, Revol JF. MSA Bull 1993;23:28–43.
[6] Sugiyama J, Harada H, Fujiyoshi Y, Uyeda N. Mokuzai Gakkaishi 1984;30:98–9.
[7] Sugiyama J, Harada H, Fujiyoshi Y, Uyeda N. Mokuzai Gakkaishi 1985;31:61–7.
[8] Sugiyama J, Harada H, Fujiyoshi Y, Uyeda N. Planta 1985;166:161–8.
[9] Sugiyama J, Harada H, Saiki H. Int J Biol Macromol 1987;9:122–30.
[10] Helbert W, Nishiyama Y, Okano T, Sugiyama J. J Struct Biol 1998;124:42–50.
[11] Helbert W, Sugiyama J, Kimura S, Itoh T. Protoplasma 1998;203:84–90.
[12] Gaill F, Persson J, Sugiyama J, Vuong R, Chanzy H. J Struct Biol 1992;109:116–28.
[13] Revol JF, Chanzy H. Biopolymers 1986;25:1599–601.
[14] Revol JF, Gardner KH, Chanzy H. Biopolymers 1988;27:345–50.
[15] Saito Y, Okano T, Chanzy H, Sugiyama J. J Struct Biol 1995;114:218–28.
[16] Helbert W, Sugiyama J. Cellulose 1998;5:113–22.
[17] Putaux J-L, Helbert W, Hÿtch MJ, Chanzy H. Proceedings of the Trinocular Congress of Electron Microscopy. Lausanne, Switzerland; 1995. p. 51.
[18] Pradère P, Revol JF, Nguyen L, St John Manley R. Ultramicroscopy 1988;25:69–80.
[19] Pradère P, Thomas EL. Ultramicroscopy 1990;32:149–68.
[20] Hÿtch MJ, Gandais M. Philos Mag A 1995;72:619–34.
[21] Hÿtch MJ. Microsc Microanal Microstruct 1997;8:41–57.
[22] Hÿtch MJ, Potez L. Philos Mag A 1997;76:1119–38.
[23] Hÿtch MJ, Snoeck E, Kilaas R. Ultramicroscopy 1998;74:131–46.
[24] Hÿtch MJ, Vernaut P, Malarria J, Portier R. Mater Sci Engng A 1999;273–275:266–70.
[25] Lyonnet R, Maurice J-L, Hÿtch MJ, Michel D, Contour J-P. Appl Surf Sci 2000;163:245–9.
[26] Atalla RH, Van der Hart DL. Science 1984;223:283–5.
[27] Sugiyama J, Vuong R, Chanzy H. Macromolecules 1991;24:4168–75.
[28] Imai T, Sugiyama J. Macromolecules 1998;31:6275–9.
[29] Yamamoto H, Horii F, Odani H. Macromolecules 1989;22:4130–2.
[30] Fukami A, Adachi K. J Electr Microsc 1965;14:112–8.
[31] Saxton WO, Pitt TJ, Horner M. Ultramicroscopy 1979;4:343–54.
[32] Misell DL. Image analysis, enhancement and interpretation. Amsterdam: North Holland; 1979.
[33] Goodman JW. Introduction to Fourier optics. New York: McGraw-Hill; 1968.
[34] Stewart M. J Electr Microsc Technique 1988;9:301–24.
[35] Bourret A, Chanzy H, Lazaro R. Biopolymers 1972;11:893–8.
[36] Gardner KH, Blackwell J. Biopolymers 1974;13:1975–2001.
[37] Sarko A, Muggli R. Macromolecules 1974;7:486–94.
[38] Cousins SK, Brown Jr RM. Polymer 1995;36:3885–8.
[39] Fujiyoshi Y, Mizusaki T, Morikawa K, Yamagishi H, Aoki Y, Kihara H, Harada Y. Ultramicroscopy 1991;38:241–51.
[40] Fujiyoshi Y. Adv Biophys 1998;35:22–80.
[41] Jakubowski U, Baumeister W, Glaeser RM. Ultramicroscopy 1989;31:351–6.